10.4 COMPARATIVE ANALYSIS OF TERMINAL WIND-SHEAR DETECTION SYSTEMS

John Y. N. Cho, Robert G. Hallowell, and Mark E. Weber
MIT Lincoln Laboratory, Lexington, Massachusetts

1. INTRODUCTION

Low-level wind shear, especially a microburst, is very hazardous to aircraft departing or approaching an airport. The danger became especially clear in a series of fatal commercial airliner accidents in the 1970s and 1980s at U.S. airports. In response, the Federal Aviation Agency (FAA) developed and deployed three ground-based low-altitude wind-shear detection systems: the Low Altitude Wind Shear Alert System (LLWAS) (Wilson and Gramzow 1991), the Terminal Doppler Weather Radar (TDWR) (Michelson et al. 1990), and the Airport Surveillance Radar Weather Systems Processor (ASR-9 WSP) (Weber and Stone 1995). Since the deployment of these sensors, commercial aircraft wind-shear accidents have dropped to near zero in the U.S. This dramatic decrease in accidents caused by wind shear appears to confirm the safety benefits provided by these detection systems. In addition, the broad area measurement capability of the TDWR and WSP provides ancillary delay reduction benefits, for example, by forecasting airport wind shifts that may require runway reconfiguration.

The current deployment strategy for these various wind-shear detection systems is justified by an earlier integrated wind-shear systems cost-benefit analysis (Martin Marietta 1994). Since that time, conditions in the national airspace system (NAS) have evolved, such as the installation of onboard predictive wind-shear detection systems in an increasing number of aircraft, improved pilot training for wind-shear hazard identification, avoidance, and recovery, and further integration of observed wind-shear data into terminal weather systems. Given the tight fiscal environment at the FAA in recent years, the cost of maintaining the wind-shear detection systems has also become an issue. All systems require periodic service life extension programs (SLEPs). In light of these developments, the FAA has tasked MIT Lincoln Laboratory to provide an updated cost-benefit study on their terminal wind-shear detection systems.

This work was sponsored by the Federal Aviation Administration under Air Force Contract No. FA8721-05-C-0002. Opinions, interpretations, conclusions, and recommendations are those of the authors and are not necessarily endorsed by the U.S. Government.

Corresponding author address: John Y. N. Cho, MIT Lincoln Laboratory, 244 Wood St., S1-659, Lexington, MA 02420-9185; e-mail: jync@ll.mit.edu.

One of the key factors in estimating the benefits of a terminal wind-shear detection system is its performance. Thus, it is necessary to quantify the wind-shear detection probability for each sensor, preferably on an airport-by-airport basis. To consider sensors that are not yet deployed, a model must be developed that takes into account the various effects that factor into the detection probability. We have developed such a model. The focus of this paper is on this model and the results obtained with it.

2. SCOPE OF STUDY

In addition to the three FAA wind-shear detection systems mentioned above, we included the Weather Surveillance Radar 1988-Doppler (WSR-88D, commonly known as NEXRAD) (Heiss et al. 1990) in this study. Although not specifically deployed to be a terminal wind-shear detection radar, the NEXRAD is a high-performance weather radar that is capable of providing useful wind-shear alerts if it is located close enough to an airport.

Furthermore, we considered new sensors in addition to the currently deployed systems. For reasons to be explained later, a Doppler lidar is expected to be a good complement to a radar for wind-shear detection. The Lockheed Martin Coherent Technologies (LMCT) Wind Tracer lidar is a commercially available product that has been operationally deployed at the Hong Kong International Airport along with a TDWR (Chan et al., 2006). It has likewise been suggested as a complementary sensor at major U.S. airports where radar alone has not been yielding satisfactory wind-shear detection performance. (The FAA has recently decided to purchase one for the Las Vegas airport.) To offer a stand-alone wind-shear detection package, LMCT has proposed an X-band radar to go along with the lidar, so we included this sensor in our analysis also.

The wind-shear phenomena for which we computed detection probabilities are the microburst and gust front. There are, in fact, other forms of hazardous wind-shear, such as gravity waves, but these are the only ones for which FAA detection requirements exist at this time. The detection coverage areas assumed was the union of the Areas Noted for Attention (ARENAs) for microbursts and an 18-km-radius circle around the airport for gust fronts. An ARENA polygon consists of the runway length plus three nautical miles final on approach and two nautical miles on departure times a width of one nautical mile. The 18-km extent of the gust-front coverage corresponds to the distance a gust front would travel at 15 m s^{-1} for 20 minutes, which is an appropriate metric for gust-front anticipation lead time in the context of airport operations.

Gust-front detection is important for delay reduction benefits. (For reference, the TDWR generates gust-front products out to 60 km from the airport.)

Table 1. Sensors vs. Airports Included in Study

Sensor	Airport (121)		
	TDWR (46)	WSP (35)	LLWAS-RS (40)
TDWR	Existing	N/A	N/A
WSP	New	Existing	N/A
LLWAS	Existing (9) New (37)	New	Existing
NEXRAD*	Existing	Existing	Existing
LMCT Lidar	New	New	New
LMCT X band	New	New	New

*Closest to airport.

Airports that presently have coverage by TDWR (46), WSP (35), and LLWAS-RS (Relocation/Sustainment) (40) were selected for this study, a total of 121 airports. Table 1 shows which sensors already exist at which airports. We did not consider the possibility of installing new TDWRs or ASR-9s due to prohibitive cost; new WSPs would only be considered for already existing ASR-9s. Deploying new or moving existing NEXRADs was not considered. (In addition to these 121 airports, we are considering adding 41 more candidate sites that currently do not have any of these three wind-shear detection systems.)

Wind-shear detection performances of sensor combinations were also analyzed (see Table 2). Again, cost-prohibitive alternatives were not considered.

Table 2. Sensor Combination vs. Site

Sensor Combination	Site
TDWR + lidar	TDWR airports
TDWR + LLWAS	TDWR airports
WSP + NEXRAD	TDWR & WSP airports
WSP + lidar	TDWR & WSP airports
WSP + LLWAS	TDWR & WSP airports
WSP + NEXRAD + lidar	TDWR & WSP airports
WSP + NEXRAD + LLWAS	TDWR & WSP airports
NEXRAD + lidar	All airports
NEXRAD + LLWAS	All airports
X-band + lidar	All airports

Note that, at the present time, NEXRADs are not suitable for microburst detection and warning, because their update rates (~5 minutes) are too slow to meet the FAA requirement. (For gust-front detection and tracking, the update rates are adequate, and the FAA already takes advantage of NEXRAD data for this purpose (Smalley et al. 2005).) Thus, even though the NEXRAD microburst detection probabilities we estimate in this study may, in some cases, appear to be acceptable, actual operational use would require that a substantially faster volume scan strategy be implemented. As a triagency radar with the FAA as a minor stakeholder, it may be problematic to prioritize the NEXRAD for terminal microburst detection in this way. In the future, an MPAR could make such multitasking a reality.

3. RADAR PERFORMANCE ANALYSIS

The radar system sensitivity was the starting point of this analysis. Shown in Table 3 are the minimum detectable dBZ at 50-km range for the four radars studied. Although these values do not include precipitation attenuation effects, in the analysis they were included at X band, where this effect can be significant.

Table 3. Minimum Detectable Reflectivity at 50 km

TDWR	-11 dBZ
NEXRAD	-10 dBZ
LMCT X band	-3 dBZ
ASR-9 WSP	7 dBZ

Radar signal detection can be noise limited or clutter limited. In the latter case, the clutter suppression capability determines the detection performance. All three existing radars (TDWR, NEXRAD, ASR-9) which have klystron transmitters, are undergoing or expected to undergo an upgrade that will bring the maximum possible clutter suppression to about 60 dB.

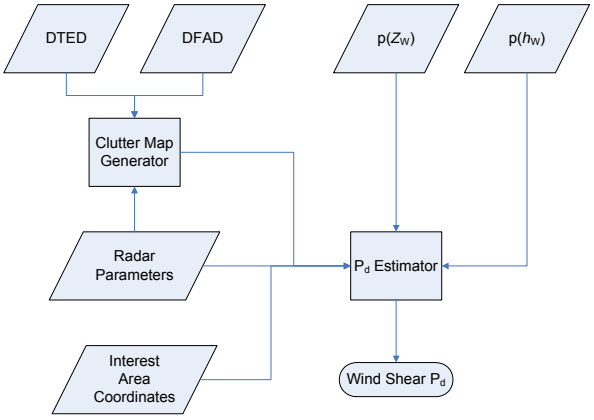

Figure 1. Flow chart of the radar wind-shear P_d performance estimator.

The ability of a radar system to detect low-altitude wind shear depends not only on the radar sensitivity and clutter suppression capability, but also on viewing geometry, clutter environment, signal processing and detection algorithm effectiveness, and the characteristics of the wind shear itself. Thus, although the system characteristics may be invariant with respect to location, there are many site-specific factors that affect the probability of detection (P_d) performance. In this study we tried to objectively account for as many of these factors as possible.

A high-level flow chart of the radar wind-shear P_d performance estimator is shown in Figure 1. For each radar at a given site, a clutter residue map (CREM) was generated using digital terrain elevation data (DTED), digital feature analysis data (DFAD), and radar characte-

ristics (Appendix A). We chose this synthetic approach over using real CREMs, because CREMs were very difficult to access in some cases (e.g., ASR-9 WSP) and the scope of this study included hypothetical installations of new systems for which, obviously, there are no existing CREMs.

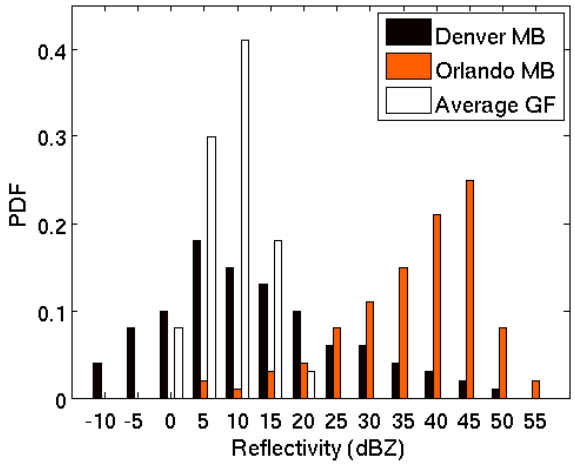

Figure 2. Empirical wind-shear reflectivity PDFs for microbursts (MB) and gust fronts (GF).

As for the probability distribution function (PDF) of the wind-shear reflectivity, $p(Z_W)$, it is based on data collected previously by the TDWR testbed radar. From these data we have direct measurements of microburst and gust-front relative reflectivity distributions from a site with a high percentage of wet microbursts (Orlando, FL) and one with predominantly dry microbursts (Denver, CO) (Weber and Troxel 1994). Figure 2 displays the observed average gust-front reflectivity PDF and both dry- and wet-site microburst PDFs. For gust fronts, the PDFs do not vary greatly with location, so we used the averaged PDF (Klingle-Wilson and Donovan 1991). For microbursts, however, the reflectivity PDF varies depending on the relative frequency of dry and wet microburst. By using the Orlando and Denver field study data as a reference we were able to generate estimates based on ancillary weather archives.

Empirical microburst-relative reflectivity data was not available for each airport; however, we did have an estimate of the overall reflectivity distribution at each site based on a one-year archive of 15-minute NEXRAD composite 2-km data (courtesy Weather Services Incorporated (WSI)). A 40-km × 40-km grid of NEXRAD reflectivities was analyzed for each site and the distribution of non-zero maximum reflectivities was utilized as an indicator of microburst reflectivity tendency. NEXRAD distributions for Denver and Orlando were used to generate a normalization to the dry and wet field study profiles, respectively. Each site's NEXRAD profile was then correlated to both the Denver and Orlando NEXRAD profiles. The correlation values were in turn used to weight each site's profile between the base line (MCO and DEN) wet and dry profiles. Figure 3 shows the conglomeration of all the airport-specific PDF distributions, while Figure 4 shows a map of the dry/wet tendency of each site. Dry sites are in the west, while wet sites are predominantly in the southeastern U.S and along the Gulf of Mexico coast.

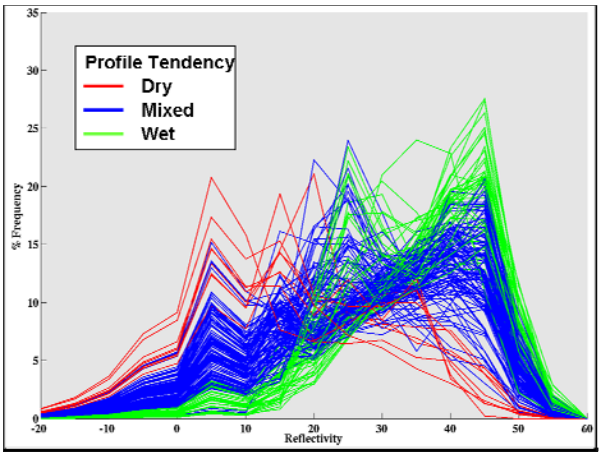

Figure 3. Estimated microburst reflectivity PDFs for all sites.

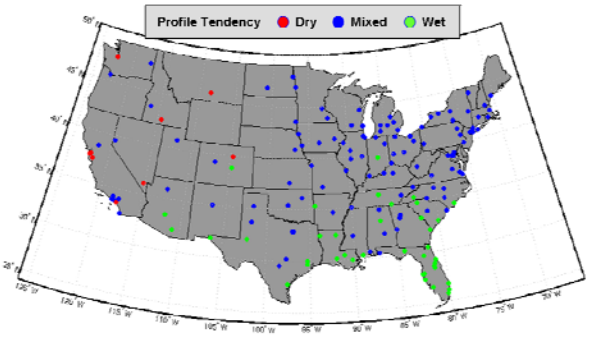

Figure 4. Map showing distribution of sites by dry/wet microburst PDF tendency.

The wind-shear outflow depth PDF, $p(h_W)$, is also an important physical parameter. Again, for gust fronts, we used a nationally averaged PDF (Wolfson et al. 1990), while for microbursts we used measured PDFs from Denver (Biron and Isaminger 1991) and Orlando (Weber et al. 1995). We then followed a procedure similar to the one described above for microburst reflectivity PDFs to generate a microburst outflow depth PDF for each airport.

The process of radar wind-shear phenomenon identification can be separated into two parts. First, the radar data are processed into sequences of volumetric reflectivity and radial velocity fields. Second, a detection algorithm searches for macroscopic wind-shear signatures in these data. Likewise, we can express the radar wind-shear P_d as the product of two parts: the radar

wind-shear visibility and the detection algorithm's "inherent" P_d. The visibility is the probability of pixel-level wind-shear signal being detected above noise and clutter averaged over interest area. The interest area is the union of ARENAs for microbursts and an 18-km radius around the airport for gust fronts. The detection algorithm P_d is the probability that the wind-shear phenomenon will be detected given perfect input data. From past performance analyses of the detection algorithms, we estimate values of 0.98 and 0.95 for the microburst and gust-front detection algorithms at a probability of false alarm (P_{fa}) of 0.1, the FAA requirement.

The visibility over the interest area, A, is given by

$$Vis = \frac{\sum_{A} V_{RF}(\boldsymbol{r})\Delta A(r) \sum_{Z_W = Z_{lo}(\boldsymbol{r})}^{Z_{hi}(\boldsymbol{r})} p(Z_W)}{\sum_{A} \Delta A(r)} \ , \qquad (1)$$

where ΔA is the incremental (pixel) area, $\boldsymbol{r}$ is the vector from the radar to ΔA, and $p(Z_W)$ is the probability distribution function of the wind-shear reflectivity Z_W (dBZ); it is normalized to sum to unity. Note that, if we take ΔA to be the area of the radar range-azimuth resolution cell, it can be replaced by r in (1), since it is only proportional to the range. The first term in (1) is the pixel-level visibility with respect to range-fold obscuration given by

$$V_{RF}(\boldsymbol{r}) = 1 - F_{RF} F_{SCR}(\boldsymbol{r}) \ , \qquad (2)$$

where F_{RF} is the probability of range-fold obscuration (see Appendix B), and the probability of the range-fold obscuration causing poor wind-shear velocity estimation is

$$F_{SCR}(\boldsymbol{r}) = \begin{cases} 1 & \text{for ASR-9} \\ \sum_{Z_W = Z_{W,\min}}^{Z_C(\boldsymbol{r}) + SCR_{thres}} p(Z_W) & \text{for other radars,} \end{cases} \qquad (3)$$

where $Z_C(\boldsymbol{r})$ (dBZ) is the clutter reflectivity and SCR_{thres} (dB) is the signal-to-clutter ratio (SCR) needed for accurate velocity-shear estimation. This expression assumes the use of spectral phase-code processing for range-fold protection, which breaks down when a clutter filter is applied simultaneously. Equation (3) gives the probability that a clutter filter would be applied, because otherwise the SCR would be too low for good velocity estimation. The value is unity for the ASR-9, because such a range-fold protection technique cannot be applied to its unevenly spaced pulse sequence with short coherent processing intervals (CPIs).

Z_{lo} (dBZ) is the equivalent reflectivity threshold above which the wind-shear reflectivity can be distinguished from "noise" due to such effects as clutter residue, receiver noise, partial beam filling, etc. This quantity is calculated from

$$Z_{lo}(\boldsymbol{r}) = \frac{\max\left[Z_{SNR}(r), Z_{CNR}(\boldsymbol{r})\right] - 2BL(r)}{\delta_{LoS}(\boldsymbol{r})} \ , \qquad (4)$$

where $\delta_{LoS}(\boldsymbol{r})$ is 1 or 0 depending on whether the radar has line-of-sight visibility to that point or not and $BL(r)$ is the beam-filling loss in dB (see Appendix B, Cho and Martin, 2007). The factor of two accounts for both the loss in signal due to partial beam filling by the desired low-altitude wind-shear signal and the increase in unwanted weather (and any other "clutter") signal in the other fraction of the beam. The receiver-noise-limited component is given by

$$Z_{SNR}(r) = Z_{\min}(r) + SNR_{CPI} + SNR_{thres} \ , \qquad (5)$$

where $Z_{min}(r)$ (dBZ) is the classical minimum detectable reflectivity, SNR_{CPI} (dB) is an adjustment factor to account for the different CPIs and pulse repetition frequencies (PRFs) used in different radars (again, see Appendix B, Cho and Martin 2007), and SNR_{thres} (dB) is the extra signal-to-noise ratio (SNR) needed for accurate velocity-shear estimation. The clutter-limited component (dBZ) is given by

$$Z_{CNR}(\boldsymbol{r}) = Z_{CREM}(\boldsymbol{r}) + SCR_{thres} \ , \qquad (6)$$

where $Z_{CREM}(\boldsymbol{r})$ is the clutter residue map (see Appendix A).

Z_{hi} (dBZ) is the equivalent reflectivity threshold above which the wind-shear reflectivity can no longer be distinguished from noise and clutter. This limiting value is taken to be infinity except for the X-band case, where attenuation due to precipitation can be severe. For this case, we posited a simple model where the reflectivity along $\boldsymbol{r}$ is equal to the wind-shear reflectivity. With that assumption we can compute a Z_{hi} threshold due to precipitation attenuation. See Appendix C for details. The X-band radar was assumed to be located in the middle of the union of the ARENAs, collocated with the lidar, at a height of 8 m above the ground.

4. LIDAR PERFORMANCE ANALYSIS

Lidars operate at much shorter wavelengths than radars, and the balance between scattering and attenuation relative to particles in the atmosphere is quite different. For a lidar, the maximum range (~12 km for the LMCT lidar) occurs under clear conditions with correspondingly low radar reflectivity values. The range generally decreases with increasing dBZ along the propagation path. Therefore, the summation over the wind-shear reflectivity PDF in computing the visibility was taken from $Z_{lo} = -\infty$ to

$$Z_{hi}(r) = \frac{Z_{\max}(r)}{\delta_{LoS}(\boldsymbol{r})} \ , \qquad (7)$$

where $Z_{max}(r)$ is the maximum detectable reflectivity for the lidar taken from the maximum detection range vs. reflectivity curve provided by LMCT. (This was a preliminary sensitivity curve, and LMCT hopes to provide us with more accurate data for the final report.) For the lidar system specifications, see Hannon (2005).

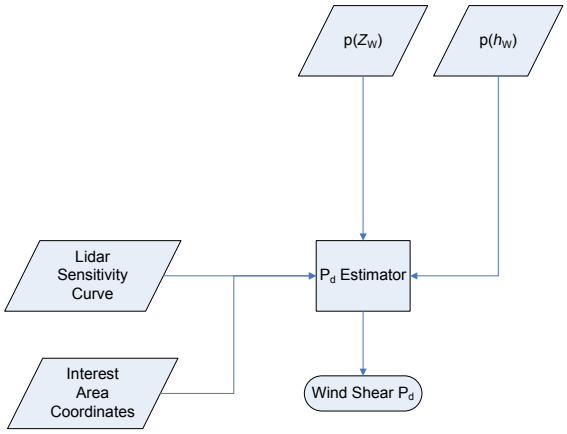

Figure 3. Flow chart of the lidar wind-shear P_d performance estimator.

Because the lidar beam is collimated, we assumed that it successfully avoids ground clutter altogether. The analysis, thus, is simplified relative to the radar performance estimator (see flow chart in Figure 3). (We also assumed that it would be sited in the center of the union of the ARENAs.) These characteristics of the lidar (maximum sensitivity at low dBZ and not being affected by clutter) make the lidar an ideal complement to a radar.

5. LLWAS PERFORMANCE ANALYSIS

The LLWAS obtains its wind measurements from anemometers mounted on towers at multiple locations in the airport vicinity. The wind-shear detection coverage provided is therefore directly dependent on the distribution of the anemometers. The number of sensors per airport is 6–10 for the LLWAS-RS and 8–32 for the LLWAS-NE++ (network expansion).

The coverage provided at each LLWAS-equipped airport is given in the data base as (nautical) miles final on arrival and departure for each runway. Since the ARENA is a one-mile-wide corridor from three miles final arrival to two miles final departure (runway inclusive), it is a simple matter to compute the LLWAS coverage as

$$Cov = \frac{\sum_{i=1}^{N_{rwy}} \left[L_{rwy}(i) + MFA(i) + MFD(i) \right]}{\sum_{i=1}^{N_{rwy}} \left[L_{rwy}(i) + 5 \right]}, \qquad (8)$$

where N_{rwy} is the number of runways, L_{rwy} is the runway length, *MFA* is the miles final arrival covered, and *MFD* is the miles final departure covered. The microburst P_d is then estimated as the product of *Cov* and the LLWAS detection algorithm P_d, which we took to be 0.97 (at P_{fa} = 0.1) (Wilson and Cole 1993).

6. SENSOR COMBINATION ANALYSIS

Fusion of data from multiple sensors has the potential to increase wind-shear detection probability. At the minimum, holes in the coverage of one sensor due to blockage, clutter residue, lack of sensitivity, etc. may be filled in by another sensor with better sensing conditions in those areas. Line-of-sight velocity fields cannot be directly merged for non-collocated sensors, but sophisticated detection algorithms that perform fuzzy logic operations on interest fields would allow merging at that level instead of at the base data level. Therefore, for radar + radar and radar + lidar combinations, we computed the visibility pixel-by-pixel (the summand associated with each $\boldsymbol{r}$ location in (1)) for each sensor and took the greater value before summing over interest region *A*.

In the case of radar(s) + LLWAS, the detection phenomenologies are independent of each other. The data on which the detection algorithms work are quite different—volumetric base data for the radar and point measurements of surface winds for the LLWAS—so they cannot be fused together in the same way as the radar and lidar data. In practice, the detection alert is issued after combining the wind-shear message outputs from the two systems (Cole 1992). Thus, we took the P_d for each sensor and combined them as P_d(combined) = 1 – [1 – P_d(radar)][1 – P_d(LLWAS)]. In theory, the false alarm rates also combine to increase in similar fashion. However, clever use of all the available contextual data can reduce false alarms (Cole and Todd 1996) so we assumed that the P_{fa} stayed constant at 0.1.

7. SELECTED RESULTS

With 121 airports, six sensors, ten sensor combinations, and two wind-shear types, the detection probability results are too numerous to list in this extended abstract. Tables of complete results will be published in an MIT Lincoln Laboratory project report in the near future. Here we give some example results.

Table 4 shows the estimated microburst detection probability for Washington-Reagan National (DCA) at P_{fa} = 10%. This airport is currently serviced by a TDWR. The color code is green for $P_d \geq 90\%$, yellow for $80\% \leq P_d < 90\%$, and red for $P_d < 80\%$, and is keyed to the FAA requirement of 90% detection rate (at a false alarm rate of 10%). For the single-sensor case, the TDWR is the only one capable of meeting the microburst detection requirement. The NEXRAD is too far away from the airport to provide satisfactory coverage in this case. The lidar detection rate is low, since DCA is a site with predominantly wet microbursts. Since this airport does not have an LLWAS, the given P_d is from the average over all existing LLWAS-RS systems.

Table 4. Microburst P_d for Washington-Reagan (DCA)

	TDWR	WSP	NEXRAD	X band	Lidar	LLWAS
Single Sensor	97%	85%	63%	88%	36%	49%
Lidar +	98%	96%	94%	95%		
LLWAS +	98%	93%	81%			

Note that these P_d values were computed for the post-upgrade TDWR, NEXRAD, and ASR-9 WSP. The first two radars are currently in the process of having their radar data acquisition (RDA) systems upgraded (Cho et al. 2005; Patel and Macemon 2004) with improvements expected in clutter suppression and range-velocity ambiguity mitigation. The ASR-9 is planned to receive an upgrade that is expected to improve system stability and, thus, clutter suppression. The P_d values corresponding to the legacy radars are somewhat lower than shown in Table 4.

As expected, combining a lidar with a radar significantly improves the microburst detection probability. In fact, even a radar less sensitive than the TDWR may be able to provide excellent microburst detection capability in the ARENAs domain in conjunction with a lidar. The LLWAS also improves the microburst P_d performance in combination with a radar, but not to the same extent as the lidar when the radar P_d is not very high. This is because LLWAS does not provide pixel-level data that can be fused with the radar data prior to processing by the detection algorithm. Note, likewise, that if the lidar and radar outputs are combined at the message level (instead of at the image pixel level as assumed in this study) then the radar + lidar P_d performance may not quite reach the levels projected by this study.

Comparison of our model results with the few case study results available generally showed good agreement. For example, the model results for the legacy (non-upgraded) TDWR at DCA yielded microburst P_d = 91%, while an empirical study gave P_d = 92% (Klingle-Wilson et al. 1997), both at P_{fa} = 10%.

Table 5 gives the microburst P_d performance estimates for Las Vegas, an airport that is currently served by a TDWR. This is one of the few airports where the TDWR has trouble meeting the 90% microburst detection requirement. It is a tough site due to the occurrence of dry microbursts as well as the presence of severe road clutter near the airport. The latter factor is believed to be the predominant cause of the TDWR's reduced performance there, because the microburst P_d for the TDWR in Denver (also a dry site) was 97%. The CREM around the Denver airport, indeed, showed little clutter residue.

Table 5. Microburst P_d for Las Vegas (LAS)

	TDWR	WSP	NEXRAD	X band	Lidar	LLWAS
Single Sensor	87%	75%	0%	63%	51%	49%
Lidar +	96%	95%	51%	81%		
LLWAS +	92%	89%	49%			

The NEXRAD does not provide any microburst coverage at LAS, and the WSP P_d performance would not be adequate on its own. The addition of a lidar would raise the microburst P_d over 90% for both the TDWR and WSP, and the addition of an LLWAS would do the same for the TDWR. (As with Washington-Reagan there is no LLWAS in Las Vegas, so we used the LLWAS-RS mean microburst P_d of 49%.)

Table 6. Gust Front P_d for Dallas-Ft. Worth (DFW)

	TDWR	WSP	NEXRAD	X band	Lidar
Single Sensor	93%	67%	91%	91%	16%
Lidar +	93%	70%	91%	92%	

Table 6 shows the estimated gust-front detection probability for Dallas-Ft. Worth at P_{fa} = 10%. There is no color code, because there is no specified FAA requirement for gust-front detection probability. This is a TDWR airport, but the NEXRAD is close enough that it would provide very good coverage for gust fronts. The lidar coverage is poor, because its maximum range is only 12 km under the best circumstances, and the gust-front interest area is an 18-km radius around the airport. The LLWAS P_d is even worse (1%), because it only provides coverage close to the airport; thus, we left it out of the table.

8. SUMMARY

As part of a comprehensive cost-benefit study, we developed an objective wind-shear detection probability estimation model for radar, lidar, and sensor combinations. This model allows a sensor- and site-specific performance analysis of deployed and future systems. The results showed that, as expected, the TDWR is the best single-sensor performer for microburst and gust-front detection among the considered wind-shear sensing systems. On its own, the ASR-9 WSP cannot provide the required 90% microburst detection probability at most airports, even after the planned upgrade to its clutter suppression capability. The NEXRAD is too far away at a majority of airports to provide adequate wind-shear detection coverage. (On the flipside, this means that there are a significant number of airports where NEXRAD data can contribute to terminal wind-shear detection, especially for gust fronts, in which case the update rate does not need to be as fast as for microbursts.) And the typical LLWAS P_d for microbursts was low (~50%), because the anemometers usually only covered a fraction of the ARENAs. In fact, the only LLWAS airport with full microburst coverage was Denver (P_d = 97%).

Although the lidar by itself did not yield impressive wind-shear detection statistics, in combination with a radar it is projected to form an optimal configuration for detection over the ARENAs. This is because the lidar excels at wind-shear detection under low reflectivity conditions when the radar signal is weak, and its collimated beam avoids ground clutter on which the radar's diverging

antenna beam impinges. An LLWAS added to a radar can also improve the microburst detection probability over the ARENAs, but not to the same extent as a lidar if the radar detection probability is not very high. Neither the lidar nor the LLWAS can contribute significantly to wide-area surveillance (beyond the ARENAs) due to their limited range.

The estimated detection probability values computed in this study will feed into the overall cost-benefit calculation for the ground-based wind-shear detection systems. The conclusions will be published in a Lincoln Laboratory project report in the near future.

9. REFERENCES

Billingsley, J. B, 2002: *Low-Angle Radar Land Clutter: Measurements and Empirical Models*. William Andrews, 722 pp.

Biron, P. J., and M. A. Isaminger, 1991: High resolution microburst outflow vertical profile data from Huntsville, Alabama, and Denver, Colorado. Project Rep. ATC-163, MIT Lincoln Laboratory, Lexington, MA, 214 pp.

Chan, P. W., C. M. Shun, and K. C. Wu, 2006: Operational LIDAR-based system for automatic windshear alerting at the Hong Kong International Airport. Preprint, *12th Conf. on Aviation, Range, and Aerospace Meteorology*, Atlanta, GA, Amer. Meteor. Soc., http://ams.confex.com/ams/pdfpapers/100601.pdf.

Cho, J. Y. N., and B. D. Martin, 2007: Technical assessment of the impact of decommissioning the TDWR on terminal weather services. Project Rep. ATC-331, MIT Lincoln Laboratory, Lexington, MA, 68 pp.

Cho, J. Y. N., G. R. Elkin, and N. G. Parker, 2005: Enhanced radar data acquisition system and signal processing algorithms for the Terminal Doppler Weather Radar. Preprints, *32nd Conf. on Radar Meteorology*, Albuquerque, NM, Amer. Meteor. Soc., P4R.8, http://ams.confex.com/ams/pdfpapers/96018.pdf.

Cole, R. E., 1992: Terminal Doppler Weather Radar/Low-Level Wind Shear Alert System integration algorithm specification version 1.1. Project Rep. ATC-187, MIT Lincoln Laboratory, Lexington, MA, 36 pp.

Cole, R. E., and R. F. Todd, 1996: A comparative performance study of TDWR/LLWAS 3 integration algorithms for wind shear detection. Preprints, *Workshop on Wind Shear and Wind Shear Alert Systems*, Amer. Meteor. Soc., Oklahoma City, OK, 43-52.

Doviak, R. J., and D. S. Zrnić, 1993: *Doppler Radar and Weather Observations*. 2nd Ed., Academic Press, 562 pp.

Hannon, S. M., 2004: Pulsed Doppler lidar for terminal area monitoring of wind and wake hazards. Preprints, *11th Conf. on Aviation, Range, and Aerospace Meteorology*, Amer. Meteor. Soc., Hyannis, MA, P4.21, http://ams.confex.com/ams/pdfpapers/87757.pdf.

Heiss W. H., D. L. McGrew, and D. Sirmans, 1990: NEXRAD: Next Generation Weather Radar (WSR-88D). *Microwave J.*, **33**, 79-98.

Klingle-Wilson, D., and M. F. Donovan, 1991: Characteristics of gust fronts. Preprints, *4th Int. Conf. on Aviation Weather Systems*, Paris, France, Amer. Meteor. Soc., 387-392.

Klingle-Wilson, D., M. Isaminger, and C. Keohan, 1997: Report on product performance for the Terminal Doppler Weather Radars (TDWRs) at Washington National Airport and Memphis and Orlando International Airports. Project Rep. ATC-246, MIT Lincoln Laboratory, Lexington, MA, 42 pp.

Martin Marietta, 1994: Wind shear systems cost-benefit and deployment study: System engineering and integration contract for implementation of the National Airspace System plan, ATC-92-1201, Martin Marietta Air Traffic Systems, 91 pp.

Michelson, M., W. W. Shrader, and J. G. Wieler, 1990: Terminal Doppler Weather Radar. *Microwave J.*, **33**, 139-148.

Patel, N. K., and R. W. Macemon, 2004: NEXRAD Open Radar Data Acquisition (ORDA) signal processing and signal path. Preprints, *20th Int. Conf. on Interactive Information and Processing Systems for Meteorology, Oceanography, and Hydrology*, Seattle, WA, Amer. Meteor. Soc., 5.4, http://ams.confex.com/ams/pdfpapers/70926.pdf.

Smalley, D. J., B. J. Bennett, and R. Frankel, 2005: MIGFA: The machine intelligent gust front algorithm for NEXRAD. Preprints, *32nd Conf. on Radar Meteorology*, Albuquerque, NM, Amer. Meteor. Soc., http://ams.confex.com/ams/pdfpapers/96098.pdf.

Tessier, Y., S. Lovejoy, and D. Schertzer, 1993: Universal multifractals: Theory and observations for rain and clouds. *J. Appl. Meteorol.*, **32**, 223-250.

Weber, M. E., and M. L. Stone, 1995: Low altitude wind shear detection using airport surveillance radars. *IEEE Aerosp. Electron. Syst. Mag.*, **10**, 3-9.

Weber, M. E., and S. W. Troxel, 1994: Assessment of the weather detection capability of an airport surveillance radar with solid-state transmitter. Project Rep. ACT-209, MIT Lincoln Laboratory, Lexington, MA, 71 pp.

Weber, M. E., M. A. Isaminger, C. Meuse, S. V. Vasiloff, and T. Shepherd, 1995: Comparative analysis of ground-based wind shear detection radars. *Proc. 1995 Int. Radar Conf.*, IEEE, Alexandria, VA, 486-495.

Weber, M. E., J. Y. N. Cho, J. S. Herd, J. M. Flavin, W. E. Benner, and G. S. Torok, 2007: The next-generation multimission U.S. surveillance radar network. *Bull. Amer. Meteor. Soc.*, **88**, 1739-1751.

Wilson, F. W., and R. E. Cole, 1993: LLWAS II and LLWAS III performance evaluation. Preprints, *5th Conf. on Aviation Weather Systems*, Amer. Meteor. Soc., Vienna, VA, 204-208.

Wilson, F. W., and R. H. Gramzow, 1991: The redesigned Low Level Wind Shear Alert System.

Preprints, *4th Int. Conf. on Aviation Weather Systems*, Paris, France, 370.

Wilson, J., D. Schertzer, and S. Lovejoy, 1991: Continuous multiplicative cascade models of rain and clouds. In *Non-Linear Variability in Geophysics*, D. Schertzer and S. Lovejoy, Eds., Kluwer Academic, pp. 185-207.

Wolfson, M., D. Klingle-Wilson, M. Donovan, J. Cullen, D. Neilley, M. Liepins, R. Hallowell, J. DiStefano, D. Clark, M. Isaminger, P. Biron, and B. Forman, 1990: Characteristics of thunderstorm-generated low altitude wind shear: A survey based on nationwide Terminal Doppler Weather Radar testbed measurements. *Proc. 29th Conf. on Decision and Control*, IEEE, Honolulu, HI, 682-688.

APPENDIX A

The synthetic clutter map generator was based on the angle-dependent model of Billingsley (2002), which assumes a Weibull distribution function for the unitless clutter coefficient σ°. The radar cross section relation between the clutter coefficient and volume reflectivity η is given by

$$\eta V = \sigma^\circ F^4 A_G \ , \tag{A1}$$

where F is the propagation factor,

$$A_G = \frac{r \Delta\phi \Delta r}{\cos\theta_{dep}} \ , \tag{A2}$$

is the ground area illuminated by the radar pulse, $\Delta\phi$ is the azimuth beamwidth, Δr is the pulse volume range extent, and the depression angle is

$$\theta_{dep} = \frac{\Delta h}{r} - \frac{r}{2R_{RE}} \ , \tag{A3}$$

where Δh is the radar antenna altitude minus the ground clutter height at vector $\boldsymbol{r}$, and R_{RE} is the usual 4/3 earth radius to account for atmospheric refraction. Since the equivalent weather reflectivity is given by

$$Z_e = \frac{\eta \lambda^4}{\pi^5 |K_w|^2} \ , \tag{A4}$$

where λ is the radar wavelength and K_w is the complex refractive index of water, the equivalent clutter reflectivity can be written (in dBZ units) as

$$Z_C(\boldsymbol{r}) = 180 + 10\log\frac{\lambda^4 B^2(\theta_{off}(\boldsymbol{r}))\sigma^\circ(\boldsymbol{r})}{\pi^5 \cos\theta_{dep}(\boldsymbol{r}) |K_w| r \Delta\theta} \ , \tag{A5}$$

where B is the one-way antenna beam power pattern (taken to be the only contributor to the propagation factor, since we do not have knowledge of the other factors), $\Delta\theta$ is the elevation beamwidth, and θ_{off} is the off-axis angle given by $\theta_{dep} + r/R_{RE}$.

To generate $\sigma^\circ(\boldsymbol{r})$ we utilized Matlab's WBLRND function, which produces random numbers following the Weibull distribution, given the two characteristic parameters, α, for scale, and β, for shape. The function call was made with

$$\alpha(\boldsymbol{r}) = \frac{10^{\sigma^\circ_W(\boldsymbol{r})/10}}{\Gamma(1 + a_W(\boldsymbol{r}))} \ , \tag{A6}$$

where Γ is the gamma function, and

$$\beta(\boldsymbol{r}) = \frac{1}{a_W(\boldsymbol{r})} \ . \tag{A7}$$

Of course, $\sigma^\circ_W(\boldsymbol{r}) = 0$ if the line of sight to location $\boldsymbol{r}$ (clutter visibility) is blocked. The quantities σ°_W and a_W are tabulated in Billingsley (2002) according to surface type, relief type, depression angle (Equation A3), radar frequency, and spatial resolution (Equation A2), following extensive clutter data collection and analysis. In order to compute the depression angle, we needed the terrain elevation, which we obtained from Level 1 DTED. To make it as realistic as possible, we also added on top of this the predominant height of above-ground structures and vegetation taken from DFAD. (This augmented elevation data was also used to determine the clutter visibility.) The relief type was determined from the standard deviation of the terrain elevation within the resolution area. Finally, the 14 DFAD radar significance factors (RSFs) were assigned to one of Billingsley's five terrain types plus a new one (metal) as shown in Table A1. See Table 4.2 in Billingsley (2002) for the corresponding values of σ°_W and a_W. For metal, we assigned σ°_W = -20 dB, and a_W = 1.8 and 1.3 at spatial resolutions of 1,000 and 1,000,000 m^2, for all radar frequencies of interest here.

Additionally, if the areal feature record indicated tree coverage greater than 50%, then the RSF-based terrain type was overridden by the forest designation.

Table A1. Assignment of Terrain Type

Terrain Type	DFAD RSF
Desert, marsh, and grassland	Desert/sand, marsh, snow/ice, water
General rural	Earthen works, soil
Forest	Trees
Mountain	Rock
Urban	Part metal, stone/brick, composition, concrete, asphalt
Metal	Metal

Since persistent moving clutter is a key data quality

issue, we kept track of the presence of roads by raising a flag in the presence of DFAD feature identification codes corresponding to elevated road, causeway, dual highway, or hard surface highway. We also computed the local orientation of the road segment, because Doppler filtering attuned to stationary clutter would fail to remove vehicular returns if their velocities had a significant component in the radar line-of-sight direction.

After the procedure outlined above was used to generate $Z_C(\boldsymbol{r})$, the clutter residue map was produced in the following manner. First, for non-road pixels, let the intermediate clutter filtered reflectivity be $Z_{CF}(\boldsymbol{r}) = Z_C(\boldsymbol{r}) - (S_{max} - L)$, where S_{max} is the maximum clutter suppression capability of the radar, L = 15 dB for the forest case, L = 10 dB for the urban and general rural case, L = 0 dB for the metal case, and L = 5 dB otherwise. The reduced clutter suppression capabilities are meant to reflect filter performance degradation due to spectral widening caused by clutter motion (e.g., wind-blown vegetation and signs, exhaust fans, etc.).

Second, for road pixels,

$$Z_{CF}(\boldsymbol{r}) = (Z_C(\boldsymbol{r}) - S_{\max})(1 - f_{\text{Road}}) + [Z_C(\boldsymbol{r}) - \min(0.2Z_C(\boldsymbol{r}), S_{\max})]f_{\text{Road}} , \quad \text{(A8)}$$

where

$$f_{\text{Road}} = \min\left[1, \max\left(0, \frac{\gamma - \gamma_0}{\gamma_1 - \gamma_0}\right)\right] , \quad \text{(A9)}$$

γ is the angle between the radar line-of-sight and the normal to the road direction, γ_0 = 60°, and γ_1 = 75°. The rationale behind this expression is that traffic flows oriented perpendicular to the radar beam would present essentially zero Doppler shift, leading to maximum clutter suppression, whereas the Doppler shifts introduced as the road orientation comes into alignment with the radar beam would cause a loss of suppression. Buildings lining the road would also tend to block the traffic from view for road directions not aligned with the line of sight (the "building canyon" effect). The study of actual road clutter data indicated that the latter factor tends to dominate. The factor 0.2, γ_0, and γ_1 were chosen based on comparisons with real data.

Third, we took the azimuthal beam-smearing effect into account. A mechanically scanned radar has an effective beamwidth, $\Delta\phi_{eff}$, that is dependent on the scan rate and dwell time in addition to the physical beamwidth (Figure 7.25, Doviak and Zrnić, 1993). The fraction of the two-way power within this effective beamwidth that is returned, not from the desired azimuthal sector, but from the one adjacent to it is approximately given by

$$p_{1s} = \left(\frac{2}{\Delta\phi_{eff}} \sqrt{\frac{\ln 2}{\pi}} \int_{-\infty}^{-\frac{\Delta\phi_{\text{sec}}}{2}} e^{-\frac{4\ln 2\, y^2}{\Delta\phi_{eff}^2}} dy \right)^2 , \quad \text{(A10)}$$

where $\Delta\phi_{sec}$ is the azimuthal sector width. This effect was incorporated into the final CREM reflectivity through the operation

$$Z_{CREM}(\boldsymbol{r}(\phi_i)) = 10\log[p_{1s}10^{Z_{CF}(\boldsymbol{r}(\phi_{i-1}))/10} + (1-2p_{1s})10^{Z_{CF}(\boldsymbol{r}(\phi_i))/10} + p_{1s}10^{Z_{CF}(\boldsymbol{r}(\phi_{i+1}))/10}] , \quad \text{(A11)}$$

where ϕ_i is the i^{th} azimuth beam position.

APPENDIX B

In order to compute the statistics of range-aliased weather signals, one needs to know the spatial variability of weather reflectivity. One can either use actual archived data or simulated data for this purpose. The advantage of the former is that the data are real; the disadvantage is that the characteristics of the radar that was used to collect the data are convolved in the results. In other words, the "actual" reflectivity data do not necessary correspond to truth given uncorrected radar-dependent effects such as beam-filling loss and precipitation attenuation. With simulated data, one can start out with the same reference reflectivity field, then add in the radar-dependent effects. This is the approach we chose.

To generate a one-dimensional (1D) reflectivity field, we appropriated a multifractal model proposed by Tessier et al. (1993). Many natural phenomena, including atmospheric processes, manifest scaling and intermittency features that are not well characterized by Gaussian statistics. The multifractal cascade model is an alternative that has had success characterizing such processes. In this model, three parameters are used to define the statistical properties of the desired (nonconservative) field: H, a measure of the deviation of the resulting field from the conserved field, c_1, the codimension of the mean process that characterizes the sparseness of the conserved field, and α_L, the Levy index (degree of multifractality). We describe the steps briefly here. Further details and explanation can be found in Wilson et al. (1991).

First, a vector is generated with length n corresponding to the number of range gates desired. The vector elements are extremal Levy random variables given by

$$y_j = \frac{\xi}{m^{1/\alpha_L}} \sum_{i=1}^{m} \left(\frac{\alpha_L}{\alpha_L - 1} - w_{ij}^{-1/a_L} \right) , \quad \text{(B1)}$$

where m is an integer sufficiently large (say, 30) for convergence, w_{ij} are elements of an m x n matrix of uniformly distributed random numbers between 0 and 1,

and

$$\xi = \left[\frac{C_1}{\Gamma(2-\alpha_L)} \right]^{1/\alpha_L} . \quad \text{(B2)}$$

Next, this subgenerator is fractionally integrated (power-law filtered in the Fourier spectral domain):

$$G_s = Y_s |k_s|^{\frac{1}{\alpha_L}-1} , \quad \text{(B3)}$$

where k is the wavenumber. Capitalizations denote the discrete Fourier transform (DFT) of their lower case counterparts, with subscript s the spectral index. Then the inverse DFT is taken and the result exponentiated,

$$q_j = \pi^{\frac{c_1}{1-\alpha_L}} e^{g_j} , \quad \text{(B4)}$$

to yield a conservative field that is dependent on both c_1 and α_L. Finally, another fractional integration using H is performed,

$$\Phi_s = Q_s |k_s|^{-H/2} , \quad \text{(B5)}$$

and the inverse DFT is taken to arrive at ϕ_j. To normalize the values to match a typical reflectivity PDF, we multiplied ϕ_j by 15. Radar reflectivity data during a convective storm were analyzed by Tessier et al. (1993) to obtain values of H = 0.32, c_1 = 0.12, and α_L = 1.4. We used these values in our simulation runs.

Starting with a 1D array of synthesized reflectivity values using the technique described above, we included effects that would diminish the reflectivity observed by a radar. (We used a 460-element array with 1-km range-gate spacing for simplicity.) First, due to Earth's curvature and finite height extent of weather, a decreasing fraction of the radar beam will be filled by weather returns with increasing range. This is the beam-filling loss effect and the way to quantify it is discussed in Appendix B of Cho and Martin (2007). To be conservative (i.e., to err on the side of more range-aliased interference) we took the weather vertical extent to be 12 km (many storms top out well below this height). Second, we accounted for atmospheric attenuation (including precipitation) effects, since this can be an important contributor to reflectivity loss, especially at X band. The two-way attenuation coefficients (dB/km) that we used were: 0.016 + 1.3 x $10^{-5}Z^{0.69}$ for S band, 0.019 + 5.0 x $10^{-5}Z^{0.75}$ for C band, and 0.028 + 1.5 x $10^{-4}Z^{0.86}$ for X band, where Z is the reflectivity in linear units. C- and S-band attenuations were considered due to the long distances (up to 460 km) involved.

We then converted the reflectivity values to SNRs. Each first-trip gate SNR was compared to all corresponding out-of-trip gate SNRs. For the ASR-9, which does not have range-fold protection, the gate was marked as obscured if the first-trip "interest area" SNR was less than 10 times the overlaid signal. For the other radars, which (will) have phase-code processing for range ambiguity resolution, the worst-case scenario was assumed, i.e., that clutter filtering was necessary. In this case, the gate was marked as obscured if the first-trip "interest area" SNR was less than the overlaid signal. If clutter filtering was ultimately not necessary, it was assumed that the range-ambiguity resolution algorithm will work well (see Equation 3). We write "interest area" in quotes, because we did not perform this simulation per radar for each site due to the unreasonable amount of time involved. Instead we used the range gates that fell within the average distances to the interest area edges. The first-trip ranges we assumed were 115 km (ASR-9 and NEXRAD), 90 km (TDWR), and 60 km (X band). The fraction of obscured gates within the "interest area" was computed, and this Monte Carlo simulation was repeated many times (we did it 1000 times) to generate the probability of range-fold obscuration, F_{RF}.

APPENDIX C

The minimum detectable reflectivity vs. range can be written in the form

$$Z_{\min}(r) = Cr^2 10^{\kappa r/10} , \quad \text{(C1)}$$

where C is a constant containing all the radar-specific parameters and κ (dB/km) is the two-way atmospheric attenuation coefficient. There is no further complication if κ is assumed to be constant, which is fine under clear-air conditions. However, κ can significantly rise over the nominal clear-air value in the presence of precipitation, especially at shorter wavelengths like X band. It is possible to relate κ to the rain rate, R (mm/h),

$$\kappa(R) = \kappa_a + a_1 R^{b_1} , \quad \text{(C2)}$$

where κ_a is the clear-air attenuation coefficient, and a_1 and b_1 are empirically fitted constants that vary with radar frequency. We use κ_a = 0.028, a_1 = 0.2 and b_1 = 1.21 for X band (Doviak and Zrnić, 1993). The rain rate, in turn, can be expressed via the Z-R relation,

$$Z(R) = a_2 R^{b_2} . \quad \text{(C3)}$$

We used a_2 = 300 and b_2 = 1.4. Putting (C2) and (C3) together, we get

$$\kappa(Z) = \kappa_a + a_1 \left(\frac{Z}{a_2} \right)^{b_1/b_2} . \quad \text{(C4)}$$

If we assume that the reflectivity is constant between the radar and the range of interest (which may be okay if the range is not very far) then (C4) inserted into (C1) yields a nonlinear equation with two possible solutions that

represent the minimum (Z_{min}) and maximum (Z_{max}) detectable reflectivity. These are the values that went into forming the “low” Z_{eff} and “high” Z_{eff} of Section 3.